

Magnetic impurity in hybrid and type-II nodal line semimetals

Xiao-Rong Yang(杨晓容), Zhen-Zhen Huang(黄真真), Wan-Sheng Wang(王万胜), and Jin-Hua Sun(孙金华)
Citation: Chin. Phys. B, 2021, 30 (**6**): 067103. DOI: 10.1088/1674-1056/abfa02
Journal homepage: http://cpb.iphy.ac.cn; http://iopscience.iop.org/cpb

What follows is a list of articles you may be interested in

Resistivity minimum emerges in Anderson impurity model modified with Sachdev-Ye-Kitaev interaction

Lan Zhang(张欄), Yin Zhong(钟寅), and Hong-Gang Luo(罗洪刚)
Chin. Phys. B, 2021, 30 (**4**): 047106. DOI: 10.1088/1674-1056/abefcb

Controllable precision of the projective truncation approximation for Green's functions

Peng Fan(范鹏), Ning-Hua Tong(同宁华)
Chin. Phys. B, 2019, 28 (**4**): 047102. DOI: 10.1088/1674-1056/28/4/047102

Site preferences of alloying transition metal elements in Ni-based superalloy: A first-principles study

Baokun Lu(路宝坤), Chong-Yu Wang(王崇愚), Zhihui Du(都志辉)
Chin. Phys. B, 2018, 27 (**9**): 097102. DOI: 10.1088/1674-1056/27/9/097102

The effects of combining alloying elements on the elastic properties of *γ*-Ni in Ni-based superalloy: High-throughput first-principles calculations

Baokun Lu(路宝坤), Chongyu Wang(王崇愚)
Chin. Phys. B, 2018, 27 (**7**): 077104. DOI: 10.1088/1674-1056/27/7/077104

Antiferromagnetism and Kondo screening on a honeycomb lattice

Lin Heng-Fu, Tao Hong-Shuai, Guo Wen-Xiang, Liu Wu-Ming
Chin. Phys. B, 2015, 24 (**5**): 057101. DOI: 10.1088/1674-1056/24/5/057101

Magnetic impurity in hybrid and type-II nodal line semimetals*

Xiao-Rong Yang(杨晓容), Zhen-Zhen Huang(黄真真), Wan-Sheng Wang(王万胜), and Jin-Hua Sun(孙金华)†

Department of Physics, Ningbo University, Ningbo 315211, *China*

(Received 25 March 2021; revised manuscript received 15 April 2021; accepted manuscript online 21 April 2021)

We study the Kondo screening of a spin-1/2 magnetic impurity in the hybrid nodal line semimetals (NLSMs) and the type-II NLSMs by using the variational method. We mainly study the binding energy and the spin–spin correlation between magnetic impurity and conduction electrons. We find that in both the hybrid and type-II cases, the density of states (DOS) is always finite, so the impurity and the conduction electrons always form bound states, and the bound state is more easily formed when the DOS is large. Meanwhile, due to the unique dispersion relation and the spin–orbit couplings in the NLSMs, the spatial spin–spin correlation components show very interesting features. Most saliently, various components of the spatial spin–spin correlation function decay with $1/r^2$ in the hybrid NLSMs, while they follow $1/r^3$ decay in the type-II NLSMs. This property is mainly caused by the special band structures in the NLSMs, and it can work as a fingerprint to distinguish the two types of NLSMs.

Keywords: hybrid nodal line semimetals, type-II nodal line semimetals, Anderson impurity, Kondo screening

PACS: 71.20.Be, 75.20.Hr, 03.65.Vf, 71.27.+a **DOI:** 10.1088/1674-1056/abfa02

1. Introduction

Topological semimetals,[1,2] represented by the Dirac semimetals (DSMs), Weyl semimetals (WSMs), and nodal line semimetals (NLSMs), are a new class of quantum matter, and have been predicted in theories and realized in experiments. Different from the DSMs/WSMs whose conduction and valence bands touch at discrete points, the NLSMs are those with the bands cross in one-dimensional lines in the momentum space.[3–5] In most studied NLSMs, the density of states (DOS) is proportional to $(E-E_{\rm F})^2$, and the NLSMs normally have drumhead-like surface states. By comparison, the DOS is proportional to $(E-E_{\rm F})$ in type-I DSMs/WSMs, and the Weyl nodes are connected by 1D Fermi arc surface states in the WSMs.[6] In analogous to the WSMs, the NLSMs can also be categorized into three types, depending on the electronic structure of the bands. To date, type-I NLSMs have been intensively studied both theoretically[7–21] and experimentally.[13,20–25] The type-II NLSMs are those with closed nodal lines but the local cones along the lines become tilted.[26,27] The hybrid NLSMs are proposed to have a partially over-tilted linear dispersion at the nodal loop. It has been reported that the type-I, type-II, and hybrid NLSMs can be realized in a realistic material, i.e., quasi-2D α-FeSi2, by strain switching.[28]

The purpose of this paper is to investigate the properties of the Kondo screening in the hybrid and the type-II NLSMs. The Kondo effect arises from the interactions between the local magnetic atom and the conduction electrons, and the Kondo effect in a normal metal has been widely studied and well understood.[29] One of the reasons that this seemingly "old" problem still receives great research interest is due to the rapidly emerging novel materials with intriguing dispersion and topological properties. In the type-I DSMs/WSMs, the DOS vanishes if the Fermi level lies right at the nodes, and the Kondo problem in such systems falls into the category of pseudo-gap Kondo problem.[30–32] The magnetic impurity and the conduction electrons form a bound state only if the hybridization between them exceeds a critical value. In Lorentz-violating host systems like tilted Dirac surface states and type-II WSMs, the formation of the impurity-conduction electron bound states is also determined by the DOS of the Fermi surface, and the spatial screening shows very rich features due to the unique dispersion relations.[33,34]

In this paper, we systematically study the binding energy and real space spin–spin correlations of a magnetic impurity in both the hybrid and type-II NLSMs. The variational method we apply has been used to study the ground state of the Kondo problem in normal metals,[35,36] antiferromagnet,[37] 2D helical metals,[38] 3D Weyl semimetals,[34,39] tilted Dirac surface states,[33] type-I NLSMs[40] and multi-WSMs,[41] and the Fermi arc surface states of WSMs.[42] Due to the intriguing nodal loop structure of the hybrid and type-II NLSMs, the Kondo screening in these systems is expected to show very interesting features.

The paper is organized as follows. We present the model and dispersion relation in Section 2. By using the model Hamiltonian we adopt, one can easily obtain different types of NLSM by tuning the parameters:[43] the system is a type-I NLSM with the tilting ratios $|m\cdot w_x|<0.5$ and $|m\cdot w_y|<0.5$, and is a type-II NLSM if $|m\cdot w_x|>0.5$ and $|m\cdot w_y|>0.5$. For the rest of the cases, the model Hamiltonian describes a hybrid

*Project supported by the Zhejiang Provincial Natural Science Foundation of China (Grant No. LY19A040003).

†Corresponding author. E-mail: sunjinhua@nbu.edu.cn

© 2021 Chinese Physical Society and IOP Publishing Ltd

NLSM. In Section 3, we apply the variational method to study the binding energy. In Section 4, we investigate the spin–spin correlation between the magnetic impurity and the conduction electrons in the hybrid and the type-II NLSMs. Finally, the discussions and conclusions are given in Section 5.

2. Anderson model Hamiltonian

We consider a spin-1/2 magnetic impurity in a 3D NLSM, and the Anderson model Hamiltonian writes

$$H = H_0 + H_d + H_{\rm V}, \tag{1}$$

in which H_0 describes the NLSM, H_d is the magnetic impurity part, and $H_{\rm V}$ is the hybridization between the magnetic impurity and the conduction electrons of the NLSM.

The NLSM is given by[3,14,15,40,43–45]

$$H_0 = \sum_{\boldsymbol{k}} c^{\dagger}_{\boldsymbol{k}} \left[h_0(\boldsymbol{k}) - \mu\right] c_{\boldsymbol{k}}, \tag{2}$$

with

$$h_0(\boldsymbol{k}) = \left(\Delta - \frac{k_i^2}{2m}\right)\tau_z\sigma_x + \nu k_z \tau_0\sigma_z - w_i k_i^2 \tau_0\sigma_0, \tag{3}$$

where $k_i^2 \equiv k_x^2 + k_y^2 + k_z^2$ and $w_i k_i^2 \equiv w_x k_x^2 + w_y k_y^2 + w_z k_z^2$, $m > 0$ is the effective mass. Δ is the radius of nodal ring projected onto the k_x–k_y plane, and we choose Δ as the energy unit. μ is the chemical potential, and ν is the Fermi velocity in the z-direction. The basis is given by $c_{\boldsymbol{k}} = \{c_{1\boldsymbol{k}\uparrow}, c_{1\boldsymbol{k}\downarrow}, c_{2\boldsymbol{k}\uparrow}, c_{2\boldsymbol{k}\downarrow}\}^{\rm T}$, where $c_{j\boldsymbol{k}\uparrow}$ $(j = 1,2)$ and $c_{j\boldsymbol{k}\downarrow}$ are the annihilation operators of spin-up and spin-down j-orbital electrons, respectively. σ_α $(\alpha = x,y,z)$ and τ_α are spin and orbital Pauli matrices, and σ_0 and τ_0 are identity matrices. In this model Hamiltonian, different types of NLSMs are conveniently obtained by tuning the tilting ratios:[43] (1) if $|m\cdot w_x| < 0.5$ and $|m\cdot w_y| < 0.5$, h_0 describes a type-I NLSM, (2) if $|m\cdot w_x| > 0.5$ and $|m\cdot w_y| > 0.5$, h_0 describes a type-II NLSM, (3) for the rest of the cases, h_0 shall be the Hamiltonian of a hybrid NLSM.

The local magnetic impurity Hamiltonian is given by

$$H_d = (\varepsilon_d - \mu)\left(d^{\dagger}_{\uparrow} d_{\uparrow} + d^{\dagger}_{\downarrow} d_{\downarrow}\right) + U n_{d\uparrow} n_{d\downarrow}, \tag{4}$$

where $d^{\dagger}_{\uparrow(\downarrow)}$ and $d_{\uparrow(\downarrow)}$ are the creation and annihilation operators of the spin-up (spin-down) state on the impurity site. ε_d and U are the impurity energy level and on-site Coulomb repulsion, respectively. The hybridization between the magnetic impurity and the host material is described by

$$H_{\rm V} = \sum_{j\boldsymbol{k}\sigma} V_{\boldsymbol{k}} (d^{\dagger}_{\sigma} c_{j\boldsymbol{k}\sigma} + {\rm H.c.}), \tag{5}$$

where $V_{\boldsymbol{k}}$ is the hybridization strength. Here we assume that the magnetic impurity is equivalently coupled to the two orbits in the NLSM for simplicity. Without loss of generally, we choose the position of the impurity as the origin $\boldsymbol{r} = 0$, such that the hybridization $V_{\boldsymbol{k}}$ is in fact independent of momentum and orbits.

One can easily obtain the single-particle eigenenergy of $h_0(\boldsymbol{k})$,

$$\varepsilon_{j\boldsymbol{k}s} = (-1)^{j+s}\sqrt{\left(\Delta - \frac{k_i^2}{2m}\right)^2 + \nu^2 k_z^2} - w_i k_i^2, \tag{6}$$

where $j = 1,2$ labels the orbits and $s = 1,2$ labels the bands. Note that the bands are two fold degenerate, and the corresponding eigenstate operators are given by

$$\gamma_{j\boldsymbol{k}s} = \Phi^*_{j1s} c_{j\boldsymbol{k}\uparrow} + \Phi^*_{j2s} c_{j\boldsymbol{k}\downarrow}, \tag{7}$$

where Φ_{j1s} and Φ_{j2s} are defined in Appendix A.

In Fig. 1, we show the band structure and DOS of the hybrid and the type-II NLSMs. The band structures shown are plotted in the k_x–k_y momentum space with $k_z = 0$.

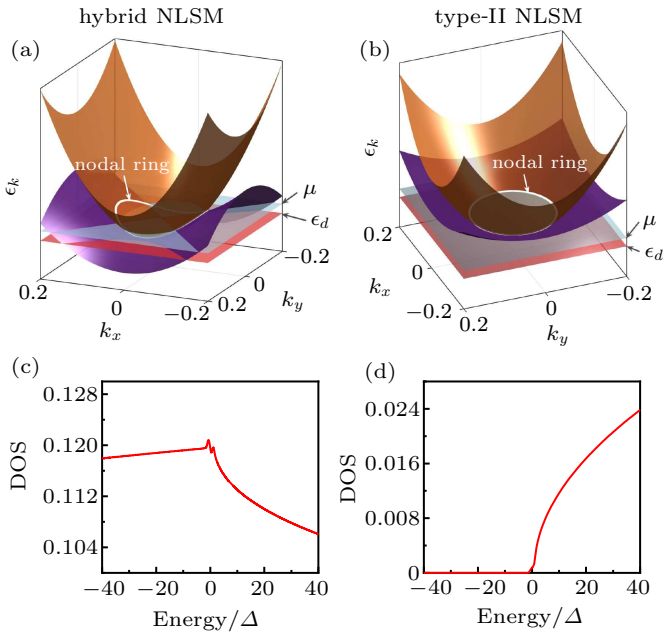


Fig. 1. Schematics of the band structure and the nodal ring of (a) a hybrid NLSM and (b) a type-II NLSM for $k_z = 0$. The nodal rings are formed by the crossing between two different bands. (c) The finite DOS per unit cell of a hybrid NLSM, and (d) the DOS of a type-II NLSM. For type-II NLSM, the lowest energy state lies at energy/$\Delta = -1$, so the DOS below $-\Delta$ is zero, and it increases monotonically with the energy.

As shown in Fig. 1(a), the nodal ring of the hybrid NLSM is formed by the crossing between the parabolic bands and the saddle-shaped bands. In the k_x–k_y plane, the nodal ring satisfies $k_x^2 + k_y^2 = 2m\Delta$, and one can see clearly that the nodal ring has energy variation along the loop, with the scale between $-2m\Delta w_x$ and $-2m\Delta w_y$. In Fig. 1(b), we show the band structure of a type-II NLSM. Different from the hybrid NLSM case, the nodal ring in the type-II NLSM lies at the energy of $-2m\Delta w_y$. In Figs. 1(c) and 1(d), we show the DOS per unit cell for the hybrid and the type-II NLSMs, respectively. The DOS is directly affected by the choice of w_i values. If we fix the value of $|m\cdot w_y| > 0.5$, in the hybrid NLSM regime, as

$|m\cdot w_x| = |m\cdot w_z|$ increases from 0.1 to about 0.5, the DOS increases accordingly. $|m\cdot w_x| = |m\cdot w_z| = 0.5$ is a critical point at which the system transits from a hybrid to a type-II NLSM. $|m\cdot w_x| = |m\cdot w_z| > 0.5$ describes the type-II regime, where the DOS results are drastically distinct from those in the hybrid regime. In the type-II NLSMs, the DOS is much lower, and most typically, the DOS below $-\Delta$ vanishes. As shown in Fig. 1(c), the DOS is larger around the charge neutrality point for the hybrid NLSM, and the DOS is always finite. Thus, one can expect that the impurity and the conduction electrons always form a bound state. For the type-II NLSM shown in Fig. 1(d), the DOS is zero if the energy is below $-\Delta$, independent of the model parameters w_i and v. For the cases that energy is above $-\Delta$, the DOS increases monotonically with the energy level. In general, the DOS around the charge neutral point is much larger in the hybrid NLSM than that in a type-II case.

3. Self-consistent calculation

We utilize the well-known trial wavefunction approach which has been used to study the ground state of the Anderson impurity problem in the conventional metal,[35,36] 2D helical metals,[38] antiferromagnets,[37] and various novel topological insulators[46] and topological semimetals.[33,34,39,42] We assume that the Coulomb repulsion U is large enough, and the impurity energy level ε_d is below the Fermi energy, so that the impurity site is always singly occupied by a local moment. For the simplest case, we first discuss the case of $H_{\rm V} = 0$, in which the magnetic impurity and the NLSM are completely decoupled from each other.

The ground state of H_0 is given by

$$|\Psi_0\rangle = \prod_{j\boldsymbol{k}s} \gamma^{\dagger}_{j\boldsymbol{k}s}|0\rangle, \tag{8}$$

where $\{j\boldsymbol{k}s\}$ means the product runs over all the states inside the Fermi surface. The total energy of the system is just the sum of the energies of the NLSM and of the bare magnetic impurity

$$E_0 = \varepsilon_d - \mu + \sum_{j\boldsymbol{k}s}(\varepsilon_{j\boldsymbol{k}s} - \mu). \tag{9}$$

Then we move on to take into account the hybridization, the trial wave function for the ground state is

$$|\Psi\rangle = \left(a_0 + \sum_{j\boldsymbol{k}s} a_{j\boldsymbol{k}s} d^{\dagger}_{j\boldsymbol{k}s}\gamma_{j\boldsymbol{k}s}\right)|\Psi_0\rangle, \tag{10}$$

where $d_{j\boldsymbol{k}s} \equiv \Phi^{*}_{j1s}d_{\uparrow} + \Phi^{*}_{j2s}d_{\downarrow}$, and a_0 and $a_{j\boldsymbol{k}s}$ are variational parameters to be determined by optimizing the ground-state energy.

The energy of the Hamiltonian in variational state $|\Psi\rangle$ is

$$E = \sum_{j\boldsymbol{k}s}[(E_0 - \varepsilon_{j\boldsymbol{k}s} + \mu)a^2_{j\boldsymbol{k}s} + 2V_k a_0 a_{j\boldsymbol{k}s} + (\varepsilon_{j\boldsymbol{k}s} - \mu)a_0^2]/\left(a_0^2 + \sum_{j\boldsymbol{k}s} a^2_{j\boldsymbol{k}s}\right). \tag{11}$$

The variational method requires that $\partial E/\partial a_0 = \partial E/\partial a_{j\boldsymbol{k}s} = 0$, from which we can obtain the following two equations:

$$\begin{aligned} \left[E - \sum_{j\boldsymbol{k}s}(\varepsilon_{j\boldsymbol{k}s} - \mu)\right] a_0 &= \sum_{j\boldsymbol{k}s} V_k a_{j\boldsymbol{k}s}, \\ (E - E_0 + \varepsilon_{j\boldsymbol{k}s} - \mu)a_{j\boldsymbol{k}s} &= V_k a_0. \end{aligned} \tag{12}$$

We defind the binding energy as $\Delta_{\rm b} = E_0 - E$, then the self-consistent equation is given by

$$(\varepsilon_d - \mu) - \Delta_{\rm b} = \sum_{j\boldsymbol{k}s} \frac{V_k^2}{\varepsilon_{j\boldsymbol{k}s} - \mu - \Delta_{\rm b}}. \tag{13}$$

By numerically solving Eq. (13), we can obtain the values of $\Delta_{\rm b}$. $\Delta_{\rm b} > 0$ means that the hybridized state has lower energy than the bare state, such that the hybridized state is more stable. In our numerical calculations, the hybridization strength is $V_k = V\Theta(\Lambda - |\varepsilon_{j\boldsymbol{k}s}|)$, where $\Theta(x)$ is the Heaviside step function and Λ is the energy cutoff. The Kondo effect is mainly influenced by the conduction electrons near the Fermi surface, so if we choose large enough values of Λ, the Kondo effect shall be insensitive to the values of the energy cutoff. The energy cutoffs for both the hybrid and type-II NLSMs are chosen as $\Lambda = 100\Delta$, where Δ is the energy unit introduced in the NLSM Hamiltonian in Eq. (3).

Figure 2 shows the dependence of the binding energy $\Delta_{\rm b}$ on the effective hybridization Γ for different values of μ. In here and below, we fix the parameters as $m = 0.005\Delta^{-1}$ Å^{-2}, $v = 10\Delta$ Å, and the impurity energy level as $\varepsilon_d = \mu - 0.01\Delta$. We use $w_x = w_z = -20\Delta$ Å^2 and $w_y = -200\Delta$ Å^2 for the hybrid NLSM, while $w_x = w_y = w_z = -200\Delta$ Å^2 for the type-II NLSM.

Note that actually the types of the NLSMs are not affect by the choice of w_z. However, by choosing $w_z = w_x$ in our numerical calculations, the system shall preserve higher symmetry property, such that the analysis on the spin–spin correlation might become clearer. As illustrated in Fig. 2(a), for a fixed value of Γ, the binding energy is the largest when $\mu = -0.6\Delta$, and the smallest if $\mu = 30\Delta$. This result is consistent with the results of DOS shown in Fig. 1(c). The binding energy is mainly influenced by the DOS at the Fermi energy, and the bound state is more easily formed when the DOS is large. For the hybrid NLSM, the DOS is always finite, so a positive binding energy always emerges for any finite values of V_k. In Fig. 2(b), we can see that for a certain value of Γ, the binding energy increases monotonically with the values of μ, which is also consistent with the DOS results given in Fig. 1(d). Notice that for relatively small Γ, the binding energies for both cases are also very small, but finite. It is well-known that the binding energy is positive only if the hybridization exceeds a

critical value if the DOS is zero, but the binding energy shall always be positive for any finite hybridization.[33,34,38,39,42,47]

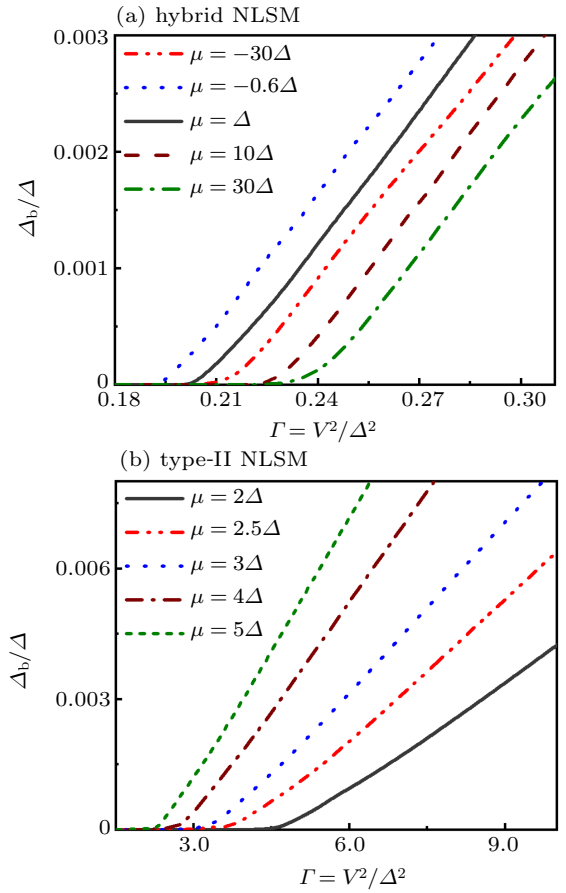


Fig. 2. Binding energy Δ_b of a magnetic impurity (a) in a hybrid NLSM and (b) in a type-II NLSM as a function of the effective hybridization Γ for different chemical potential μ.

4. Spin–spin correlation

In this section, we study the spatial spin–spin correlation between the magnetic impurity and the conduction electrons in the hybrid and type-II NLSMs. The spin operator of the magnetic impurity is defined as $\boldsymbol{S}_d=\frac{1}{2}d^\dagger\boldsymbol{\sigma}d$, while the spin of the conduction electrons is given by $\boldsymbol{S}_c=\boldsymbol{S}_{c_1}+\boldsymbol{S}_{c_2}=\frac{1}{2}c_1^\dagger\boldsymbol{\sigma}c_1+\frac{1}{2}c_2^\dagger\boldsymbol{\sigma}c_2$, where the numbers 1 and 2 label the two different orbits in the NLSM. $\boldsymbol{\sigma}$ is the Pauli matrix, and $d=\{d_\uparrow,d_\downarrow\}^{\mathrm{T}}$, $c_1=\{c_{1\uparrow},c_{1\downarrow}\}^{\mathrm{T}}$, and $c_2=\{c_{2\uparrow},c_{2\downarrow}\}^{\mathrm{T}}$ are the annihilation operators at the impurity site and in the two orbits in the NLSMs.

The spatial spin–spin correlation function is given by

$$J_{uv}(\boldsymbol{r})=\langle S_c^u(\boldsymbol{r})S_d^v(0)\rangle, \tag{14}$$

where $u,v=x,y,z$ are the spin indices and $\langle\cdots\rangle$ denotes the ground state average. One can see that the NLSM Hamiltonian given in Eq. (3) is invariant under combined operations $\mathcal{T}R^y(\pi)$, $\mathcal{T}R^z(\pi)$, and $R^x(\pi)$, where $\mathcal{T}$ is the time-reversal operation and $R^u(\pi)$ $(u=x,y,z)$ is the rotation of angle π about the u-axis. For example, considering the invariance under the combined operation $\mathcal{T}R^y(\pi)$, one can prove that $J_{uv}(\boldsymbol{r})=J_{uv}(\tilde{\boldsymbol{r}})$ in the x–y plane, where $\tilde{\boldsymbol{r}}=(-x,y,z)$.

The diagonal terms and the non-zero off-diagonal terms of the spin–spin correlation function are given by

$$\begin{aligned}
J_{zz}(\boldsymbol{r}) &= -\frac{1}{4}\sum_j(|A_{j11}|^2-|A_{j12}|^2-|A_{j21}|^2+|A_{j22}|^2),\\
J_{xx}(\boldsymbol{r}) &= -\frac{1}{2}\sum_j[\mathrm{Re}(A_{j12}A_{j21}^*)+\mathrm{Re}(A_{j11}A_{j22}^*)],\\
J_{yy}(\boldsymbol{r}) &= \frac{1}{2}\sum_j[\mathrm{Re}(A_{j12}A_{j21}^*)-\mathrm{Re}(A_{j11}A_{j22}^*)],\\
J_{xy}(\boldsymbol{r}) &= -\frac{1}{2}\sum_j[\mathrm{Im}(A_{j12}A_{j21}^*)-\mathrm{Im}(A_{j11}A_{j22}^*)],\\
J_{xz}(\boldsymbol{r}) &= -\frac{1}{2}\sum_j[\mathrm{Re}(A_{j11}A_{j21}^*)-\mathrm{Re}(A_{j12}A_{j22}^*)],\\
J_{yz}(\boldsymbol{r}) &= -\frac{1}{2}\sum_j[\mathrm{Im}(A_{j11}A_{j21}^*)-\mathrm{Im}(A_{j12}A_{j22}^*)],\\
J_{yx}(\boldsymbol{r}) &= -\frac{1}{2}\sum_j[\mathrm{Im}(A_{j12}A_{j21}^*)+\mathrm{Im}(A_{j11}A_{j22}^*)],\\
J_{zx}(\boldsymbol{r}) &= -\frac{1}{2}\sum_j[\mathrm{Re}(A_{j12}A_{j11}^*)-\mathrm{Re}(A_{j22}A_{j21}^*)],\\
J_{zy}(\boldsymbol{r}) &= -\frac{1}{2}\sum_j[\mathrm{Im}(A_{j12}A_{j11}^*)-\mathrm{Im}(A_{j22}A_{j21}^*)],
\end{aligned} \tag{15}$$

where $A_{j\tilde{s}_1\tilde{s}_2}(\boldsymbol{r})=\sum_{\boldsymbol{k}s}\mathrm{e}^{-\mathrm{i}\boldsymbol{k}\cdot\boldsymbol{r}}a_{j\boldsymbol{k}s}\Phi^*_{j\tilde{s}_1s}\Phi_{j\tilde{s}_2s}$ with $\tilde{s}_1,\tilde{s}_2=1,2$. Since $\Phi_{j\tilde{s}_1s}$ and $\Phi_{j\tilde{s}_2s}$ are real, $A_{j\tilde{s}_1\tilde{s}_2}(\boldsymbol{r})=A_{j\tilde{s}_2\tilde{s}_1}(\boldsymbol{r})$. Thus we get $J_{xy}(\boldsymbol{r})=-J_{yx}(\boldsymbol{r})$, $J_{xz}(\boldsymbol{r})=J_{zx}(\boldsymbol{r})$, and $J_{yz}(\boldsymbol{r})=-J_{zy}(\boldsymbol{r})$.

The magnitude of Δ_b depends directly on the DOS at the Fermi energy. In a hybrid or a type-II NLSM, the DOS is finite around the nodal ring, so Δ_b always takes a positive solution. It indicates that the localized state and the conduction electrons always form bound states for arbitrarily small $V_{\boldsymbol{k}}$. On the other hand, once the bound states are formed, the spatial spin–spin correlation functions are not much affected by the choice of μ except for the magnitude. In the present paper, the spin–spin correlation function of the hybrid NLSM is evaluated for $\mu=\Delta$ (around the center of the hybrid nodal ring energy range), while for type-II NLSM $\mu=2\Delta$ (at the nodal ring energy) is used. In fact, we also calculate the spin–spin correlation for other values of μ (not shown), the decay rate and the spatial patterns of various components of the spin–spin correlation turn out to be qualitatively the same. The changes of w_i naturally lead to the changes in Δ_b. However, we may fix the value of Δ_b in the spin–spin correlation calculations to mainly concentrate on the spatial patterns. Our typical parameter choice is $\Delta_b=10\Delta$, and $V=(11/\sqrt{2})\Delta$. The spin–spin correlation decays very fast in the real space, so in order to investigate the spin–spin correlation more clearly, $r^nJ_{uv}(\boldsymbol{r})$ instead of $J_{uv}(\boldsymbol{r})$ are plotted in Figs. 3–7. $n=2$ in the hybrid NLSM and $n=3$ in the type-II NLSM, depending on the spatial decay rate in two different systems. By substituting the

expressions of $\Phi_{j\tilde{s}_i s}$ ($\tilde{s}_i = \tilde{s}_1, \tilde{s}_2$) given in Appendix A, we have

$$A_{j11}(\boldsymbol{r}) = \sum_{\boldsymbol{k}} \mathrm{e}^{-\mathrm{i}\boldsymbol{k}\cdot\boldsymbol{r}}(a_{j\boldsymbol{k}1}\Phi^*_{j11}\Phi_{j11} + a_{j\boldsymbol{k}2}\Phi^*_{j12}\Phi_{j12}),$$
$$A_{j22}(\boldsymbol{r}) = \sum_{\boldsymbol{k}} \mathrm{e}^{-\mathrm{i}\boldsymbol{k}\cdot\boldsymbol{r}}(a_{j\boldsymbol{k}1}\Phi^*_{j21}\Phi_{j21} + a_{j\boldsymbol{k}2}\Phi^*_{j22}\Phi_{j22}). \quad (16)$$

One can easily prove that $A_{j11}(\boldsymbol{r}) = A_{j22}(\boldsymbol{r})$, so $J_{yy}(\boldsymbol{r}) = J_{zz}(\boldsymbol{r})$. Thus we only show the term of the spin–spin correlation $r^n J_{yy}(\boldsymbol{r})$ in Figs. 3–7.

In Fig. 3, one can see that the spin–spin correlation functions along all the three spatial directions, x-, y- and z-axes decay with power law $1/r^2$. The momentum cutoff k_c is chosen with respect to the energy cutoff Λ. The major difference is that the off-diagonal terms are all zero along the x- and y-directions, but one off-diagonal term $J_{xy}(\boldsymbol{r})$ is finite along the z-axis.

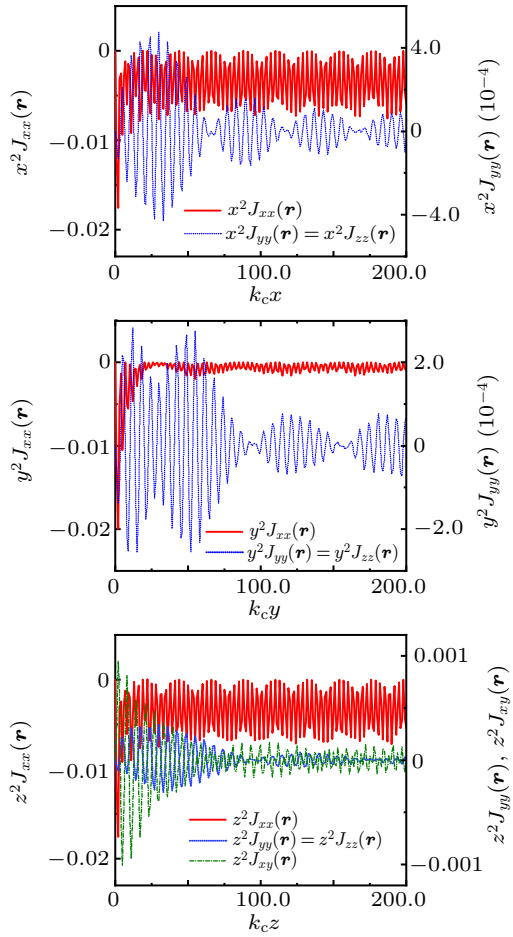


Fig. 3. Spin–spin correlations in a hybrid NLSM decay at the power of $1/r^2$ along the x-, y-, and z-axes at long distance. $r^2J_{xx}(\boldsymbol{r})$ along the x-axis decays in the same way as that along the z-axis. k_c is the momentum cutoff chosen with respect to the energy cutoff Λ.

Figure 4 shows the spin–spin correlations function of the type-II NLSM along the y- and z-axes. Because $w_x = w_y$, we shall have $A_{j\tilde{s}_1\tilde{s}_2}(\boldsymbol{r}) = A_{j\tilde{s}_1\tilde{s}_2}(\sqrt{x^2+y^2}, z)$, one can prove that $J_{uv}(\boldsymbol{r})$=$J_{uv}(\sqrt{x^2+y^2}, z)$, indicating that the spatial spin–spin correlation in the x–y plane preserves the rotational symmetry. The spatial spin–spin correlations shall be exactly the same for the x- and y-axes, so we only show the y-axis results in Fig. 4. Distinct from the hybrid case shown in Fig. 3, all the off-diagonal terms along the x-, y-, and z-axes are zero, and the spin–spin correlations function decays as the power of $1/r^3$ in the type-II NLSM.

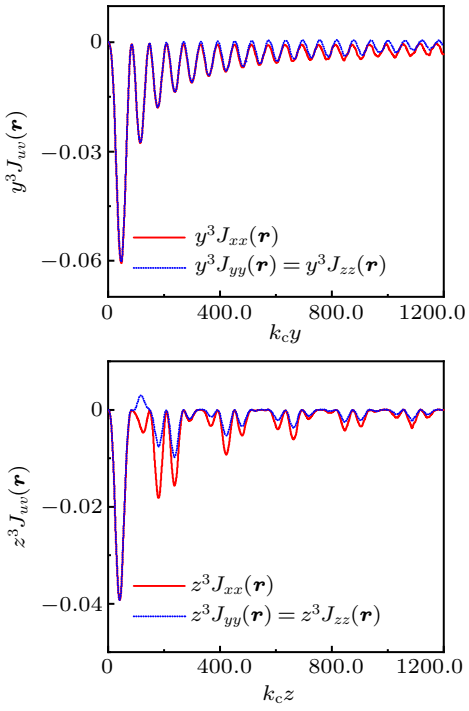


Fig. 4. Various components of the spin–spin correlation function in a type-II NLSM decay at the power of $1/r^3$ along the three coordinate axes at long distance. Due to the rotational symmetry about the z-axis, $J_{uv}(x)$ is exactly the same as $J_{uv}(y)$.

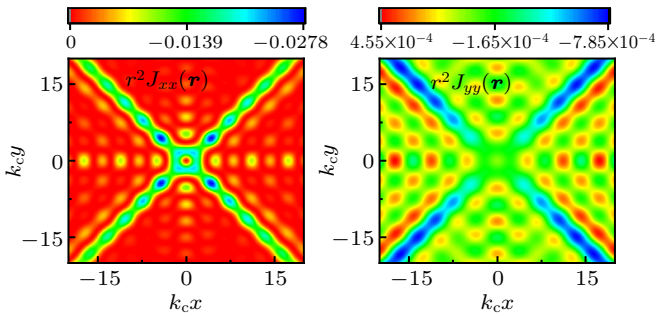


Fig. 5. Terms of the spin–spin correlation $r^2J_{uv}(\boldsymbol{r})$ $(u, v = x, y, z)$ in the x–y coordinate plane for a hybrid NLSM. All the off-diagonal terms vanish in the x–y plane, so they are not shown.

The spin–spin correlations between the local magnetic impurity and the conduction electrons in different 2D coordinate planes are given in Figs. 5–7. In Fig. 5 we show the spin–spin correlations between the magnetic impurity and the conduction electrons in a hybrid NLSM in the x–y plane. The tilting ratios of the NLSM model Hamiltonian are $|m \cdot w_x| = |m \cdot w_z| = 0.1$ and $|m \cdot w_y| = 1$. The system is invariant under the operations of $\mathcal{T}R^y(\pi)$ or $R^x(\pi)$, so the spin–spin correlations in the x–y plane is symmetric with respect to the x- and y-axes. $J_{xx}(\boldsymbol{r})$ is always antiferromagnetic and oscillates as $|\boldsymbol{r}|$ increases. The other two diagonal terms have the relation

$J_{yy}(\boldsymbol{r}) = J_{zz}(\boldsymbol{r})$, and all the off-diagonal terms vanish in this plane. In fact, the contributions from two different NLSM orbits cancel each other for $J_{xz}(\boldsymbol{r})$ and $J_{yz}(\boldsymbol{r})$. For $J_{xy}(\boldsymbol{r})$, considering the symmetry operations, we can get $J_{xy}(x,y) = -J_{xy}(-x,y) = J_{xy}(-x,-y) = -J_{xy}(x,-y) = 0$, which is different from x–z and y–z plans.

In Fig. 6, we show the spin–spin correlations in the (a) x–z plane (top row) and (b) y–z plane (bottom row). Note that the off-diagonal term $J_{xy}(\boldsymbol{r})$ is nonzero in both planes. In the x–z plane, according to symmetry under the combined operation $\mathcal{T}R^z(\pi)$, one can easily know that $J_{xy}(x,z) = J_{xy}(-x,z)$, such that $r^2 J_{xy}(x,z)$ is symmetric with respect to the y-axis. Considering the operation $R^x(\pi)$, $J_{xy}(x,z) = -J_{xy}(x,-z)$, and if $z = 0$ the off-diagonal term $J_{xy}(x,z)$ is always zero. Analogously, $J_{xy}(y,z)$ is always zero if $z = 0$, which is caused by the symmetries about x-axis in the y–z plane plus the two combined operations $\mathcal{T}R^y(\pi)$ and $\mathcal{T}R^z(\pi)$. The diagonal terms in the x–z plane and y–z plane are symmetric with respect to the axes. Due to the unique band structure and the spin–orbit coupling, the spin–spin correlations shows strong anisotropy in different planes, and among the different diagonal components.

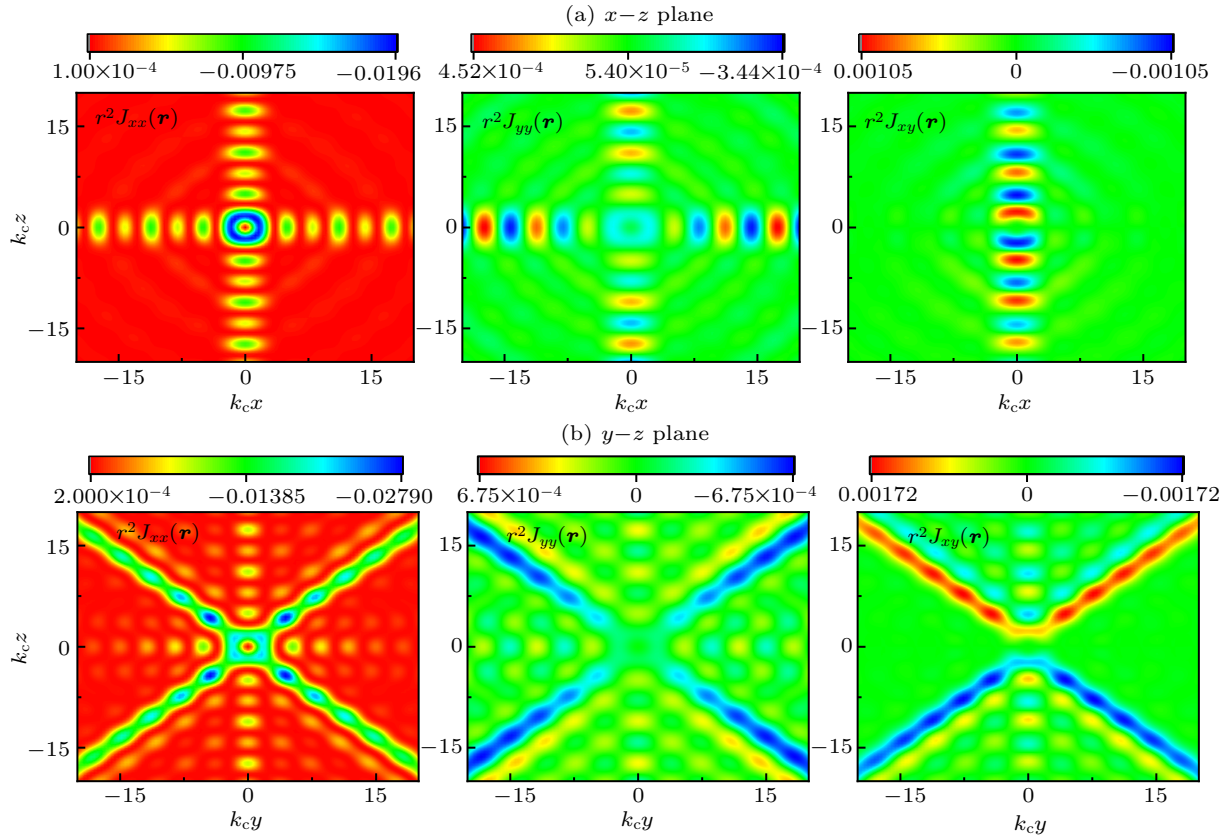


Fig. 6. The $r^2 J_{uv}(\boldsymbol{r})$ $(u,v = x,y,z)$ in the (a) x–z plane and (b) y–z plane for a hybrid NLSM. All the other off-diagonal components not shown are zero.

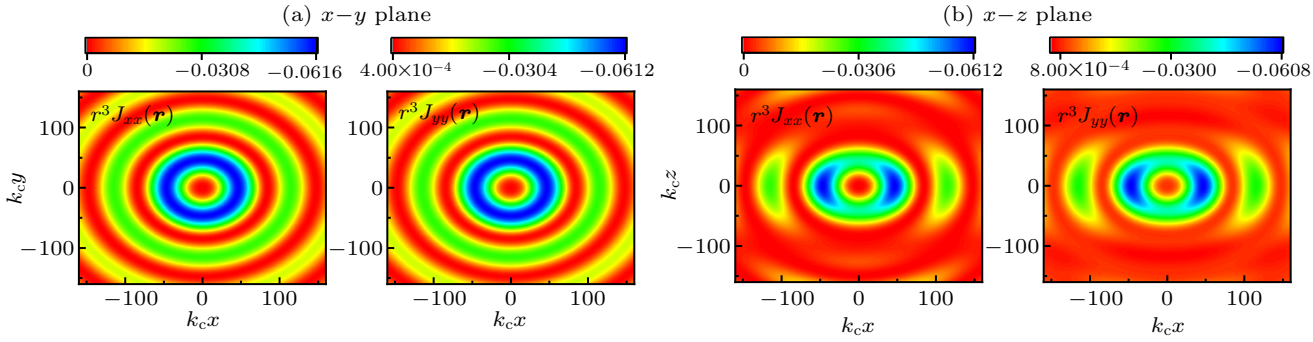


Fig. 7. The diagonal terms of the spin–spin correlation $r^3 J_{uv}(\boldsymbol{r})(u,v = x,y,z)$ of the type-II NLSM in (a) x–y plane and (b) x–z plane. All the off-diagonal terms vanish in the type-II NLSM.

Figure 7 shows the diagonal components of the spin–spin correlations between a magnetic impurity and a type-II NLSM electrons in the x–y and x–z planes. Considering the rotational symmetry, $J_{uv}(\boldsymbol{r}) = J_{uv}(\sqrt{x^2+y^2}, z)$ and $J_{uv}(x,z) = J_{uv}(y,z)$. We only show the results in the x–z plane. The tilting ratios describing this system are set as $|m \cdot w_x| = 1$ and $|m \cdot w_y| = 1$.

Note that the type-II NLSM is also invariant under the operations $\mathcal{T}R^y(\pi)$, $\mathcal{T}R^z(\pi)$, and $R^x(\pi)$. Distinct from the hybrid NLSM case, all the off-diagonal terms in all the three planes are zero. $J_{xz}(\boldsymbol{r})$ vanishes because the contributions from the two orbits in the type-II NLSM cancel each other, while $J_{xy}(\boldsymbol{r})$ and $J_{yz}(\boldsymbol{r})$ are zero in each orbit. $J_{xx}(\boldsymbol{r})$ is always negative in the two planes, the correlation is antiferromagnetic and oscillates as $|\boldsymbol{r}|$ increases. The other components of the spin–spin correlations in three planes oscillate with respect to the real-space coordinate. For both the x–y and x–z planes, we have $J_{yy}(\boldsymbol{r}) = J_{zz}(\boldsymbol{r}) \neq J_{xx}(\boldsymbol{r})$.

5. Conclusions

In summary, we study the Kondo screening effect of a spin-1/2 magnetic impurity in the hybrid and type-II NLSMs. The NLSM model Hamiltonian we adopt has the advantage that by expediently tuning the model parameters different types of NLSMs are realized: (a) a type-I NLSM if $|m\cdot w_x| < 0.5$ and $|m\cdot w_y| < 0.5$, (b) a type-II NLSM if $|m\cdot w_x| > 0.5$ and $|m\cdot w_y| > 0.5$, (c) a hybrid NLSM for the rest of the cases. In our calculation, $|m\cdot w_x| = |m\cdot w_z| = 0.1$ and $|m\cdot w_y| = 1$ are used for a hybrid case, while $|m\cdot w_x| = |m\cdot w_y| = |m\cdot w_z| = 1$ are used for a type-II case.

The Kondo effect of a single magnetic impurity in a type-I NLSM has been studied, and it has been reported that when the chemical potential lies at the nodal loop, the magnetic impurity and the conduction electrons form bound states only if their coupling exceeds a critical value and the spatial decay ratio is either proportional to $1/r^2$ or $1/r^3$, depending on the real space directions.[40]

Distinct from the type-I case already studied, in the hybrid and type-II NLSMs discussed in this paper, the DOS is always significant, so the magnetic impurity and the conduction electrons always form bound states. The DOS of the hybrid case is much larger than that of the type-II case, so in general the binding energy takes larger values in the hybrid case.

The spatial spin–spin correlations between the magnetic impurity and the conduction electrons shows anisotropic patterns, which can be discussed using the symmetry analysis of the host materials, and decays with r^{-2} in hybrid NLSMs, and follows r^{-3} decay in type-II NLSMs. This behavior is independent of the chemical potential and DOS, and is also independent of real space axis directions. The r^{-3} decay behavior in our type-II NLSM Hamiltonian is qualitatively consistent with the results obtained in the type-I case,[40] considering that the dispersion relation contains quadratic terms along the k_z-axis. However, the r^{-2} decay rate observed in the hybrid NLSM is much distinct from the type-I and type-II cases. Overall, the spatial decays in the hybrid and type-II NLSMs are different from that in a nomal metal,[48,49] and in the DSMs/WSMs.[39] This interesting feature can possibly work as a fingerprint to distinguish different types of NLSMs in experiments.

Appendix A

According Eq. (3), by diagonalizing this Hamiltonian, we obtain the eigenvalues

$$\varepsilon_{j\boldsymbol{k}s} = (-1)^{j+s}\sqrt{\left(\Delta - \frac{k_i^2}{2m}\right)^2 + v^2k_z^2} - w_i k_i^2, \tag{A1}$$

where $j, s = 1, 2$, and the bands are two-fold degenerate. For $j = 1$ and $s = 1$, the corresponding eigen-vectors are

$$\Phi_{11} = \frac{vk_z + \sqrt{(\Delta - \frac{k_i^2}{2m})^2 + v^2k_z^2}}{\sqrt{\left(vk_z + \sqrt{(\Delta - \frac{k_i^2}{2m})^2 + v^2k_z^2}\right)^2 + \left(\Delta - \frac{k_i^2}{2m}\right)^2}},$$

$$\Phi_{21} = \frac{\Delta - \frac{k_i^2}{2m}}{\sqrt{\left(vk_z + \sqrt{(\Delta - \frac{k_i^2}{2m})^2 + v^2k_z^2}\right)^2 + \left(\Delta - \frac{k_i^2}{2m}\right)^2}},$$

$$\Phi_{31} = \Phi_{41} = 0. \tag{A2}$$

For $j = 1$ and $s = 2$,

$$\Phi_{12} = \frac{vk_z - \sqrt{(\Delta - \frac{k_i^2}{2m})^2 + v^2k_z^2}}{\sqrt{\left(vk_z - \sqrt{(\Delta - \frac{k_i^2}{2m})^2 + v^2k_z^2}\right)^2 + \left(\Delta - \frac{k_i^2}{2m}\right)^2}},$$

$$\Phi_{22} = \frac{\Delta - \frac{k_i^2}{2m}}{\sqrt{\left(vk_z - \sqrt{(\Delta - \frac{k_i^2}{2m})^2 + v^2k_z^2}\right)^2 + \left(\Delta - \frac{k_i^2}{2m}\right)^2}},$$

$$\Phi_{32} = \Phi_{42} = 0. \tag{A3}$$

For $j = 2$ and $s = 2$,

$$\Phi_{13} = \Phi_{23} = 0,$$

$$\Phi_{33} = \frac{-vk_z - \sqrt{(\Delta - \frac{k_i^2}{2m})^2 + v^2k_z^2}}{\sqrt{\left(vk_z + \sqrt{(\Delta - \frac{k_i^2}{2m})^2 + v^2k_z^2}\right)^2 + \left(\Delta - \frac{k_i^2}{2m}\right)^2}},$$

$$\Phi_{43} = \frac{\Delta - \frac{k_i^2}{2m}}{\sqrt{\left(vk_z + \sqrt{(\Delta - \frac{k_i^2}{2m})^2 + v^2k_z^2}\right)^2 + \left(\Delta - \frac{k_i^2}{2m}\right)^2}}. \tag{A4}$$

For $j = 2$ and $s = 1$,

$$\Phi_{14} = \Phi_{24} = 0,$$

$$\Phi_{34} = \frac{-vk_z + \sqrt{(\Delta - \frac{k_i^2}{2m})^2 + v^2k_z^2}}{\sqrt{\left(vk_z - \sqrt{(\Delta - \frac{k_i^2}{2m})^2 + v^2k_z^2}\right)^2 + \left(\Delta - \frac{k_i^2}{2m}\right)^2}},$$

$$\Phi_{44} = \frac{\Delta - \frac{k_i^2}{2m}}{\sqrt{\left(vk_z - \sqrt{(\Delta - \frac{k_i^2}{2m})^2 + v^2k_z^2}\right)^2 + \left(\Delta - \frac{k_i^2}{2m}\right)^2}}. \tag{A5}$$

The transform matrix is defined as

$$S=\begin{pmatrix}\Phi_{11} & \Phi_{12} & 0 & 0\\ \Phi_{21} & \Phi_{22} & 0 & 0\\ 0 & 0 & \Phi_{33} & \Phi_{34}\\ 0 & 0 & \Phi_{43} & \Phi_{44}\end{pmatrix}, \tag{A6}$$

and since S is a unitary matrix, we have $S^{\dagger}=S^{-1}$. Then the Hamiltonian can be written as

$$\begin{aligned}H_0(\boldsymbol{k}) &= \sum_{\boldsymbol{k}} c^{\dagger}_{\boldsymbol{k}}(h_0(\boldsymbol{k})-\mu)c_{\boldsymbol{k}}\\ &= \sum_{\boldsymbol{k}} c^{\dagger}_{\boldsymbol{k}} S(S^{\dagger}(h_0(\boldsymbol{k})-\mu)S)S^{\dagger}c_{\boldsymbol{k}},\end{aligned} \tag{A7}$$

where

$$h_0(\boldsymbol{k})=\left(\Delta-\frac{k_i^2}{2m}\right)\tau_z\sigma_x+vk_z\tau_0\sigma_z-w_ik_i^2\tau_0\sigma_0.$$

Because the two orbits in the NLSM are not coupled with each other, for the convenience of expression, we re-define the non-zero diagonal blocks of the S matrix as two 2×2 matrices

$$\begin{aligned}&\Phi_{111}=\Phi_{11},\ \Phi_{112}=\Phi_{12},\ \Phi_{121}=\Phi_{21},\ \Phi_{122}=\Phi_{22};\\ &\Phi_{211}=\Phi_{33},\ \Phi_{212}=\Phi_{34},\ \Phi_{221}=\Phi_{43},\ \Phi_{222}=\Phi_{44}.\end{aligned} \tag{A8}$$

Then we obtain $\Phi_{j\tilde{s}_i s}$ where $\tilde{s}_i=\tilde{s_1},\tilde{s_2}$. Then the diagonal operators are given by

$$\gamma_{j\boldsymbol{k}s}=\Phi^{*}_{j1s}c_{j\boldsymbol{k}\uparrow}+\Phi^{*}_{j2s}c_{j\boldsymbol{k}\downarrow}. \tag{A9}$$

According Eq. (5), we can obtain the transformation of d-operators as

$$d_{j\boldsymbol{k}s}=\Phi^{*}_{j1s}d_{\uparrow}+\Phi^{*}_{j2s}d_{\downarrow}. \tag{A10}$$

References

[1] Armitage N P, Mele E J and Vishwanath A 2018 *Rev. Mod. Phys.* **90** 015001
[2] Bernevig A, Weng H M, Fang Z and Dai X 2018 *J. Phys. Soc. Jpn.* **87** 041001
[3] Fang C, Chen Y G, Kee H Y and Fu L 2015 *Phys. Rev. B* **92** 081201
[4] Fang C, Weng H M, Dai X and Fang Z 2016 *Chin. Phys. B* **25** 117106
[5] Yu R, Fang Z, Dai X and Weng H M 2017 *Front. Phys.* **12** 127202
[6] Hu J, Xu S Y, Ni N and Mao Z Q 2019 *Annu. Revi. Mater. Res.* **49** 207-252
[7] Heikkilä T T and Volovik G E 2011 *JETP Lett.* **93** 59
[8] Burkov A A, Hook M D and Balents L 2011 *Phys. Rev. B* **84** 235126
[9] Teo J C Y, Schnyder A P and Ryu S 2016 *Rev. Mod. Phys.* **88** 035005
[10] Chan Y H, Chiu C K, Chou M Y and Schnyder A P 2016 *Phys. Rev. B* **93** 205132
[11] Chiu C K and Schnyder A P 2014 *Phys. Rev. B* **90** 205136
[12] Ali M N, Gibson Q D, Klimczuk T and Cava R J 2014 *Phys. Rev. B* **89** 020505
[13] Xie L S, Schoop L M, Seibel E M, Gibson Q D, Xie W W and Cava R J 2015 *APL Mater.* **3** 083602
[14] Kim Y, Wieder B J, Kane C L and Rappe A M 2015 *Phys. Rev. Lett.* **115** 036806
[15] Yu R, Weng H M, Fang Z, Dai X and Hu X 2015 *Phys. Rev. Lett.* **115** 036807
[16] Bian G, Chang T R, Zheng H, *et al.* 2016 *Phys. Rev. B* **93** 121113
[17] Weng H M, Dai X and Fang Z 2016 *J. Phys.: Condens. Matter* **28** 303001
[18] Huang H Q, Liu J P, David V and Duan W H 2016 *Phys. Rev. B* **93** 201114
[19] Mullen K, Uchoa B and Glatzhofer D T 2015 *Phys. Rev. Lett.* **115** 026403
[20] Bian G, Chang T R, Sankar R, *et al.* 2016 *Nat. Commun.* **7** 10556
[21] Schoop L M, Ali M N, Straßer C, *et al.* 2016 *Nat. Commun.* **7** 11696
[22] Neupane M, Belopolski I, Hosen M M, *et al.* 2016 *Phys. Rev. B* **93** 201104
[23] Wu Y, Wang L L, Mun E, *et al.* 2016 *Nat. Phys.* **12** 667
[24] Hu J, Tang Z J, Liu J Y, *et al.* 2016 *Phys. Rev. Lett.* **117** 016602
[25] Takane D, Wang Z W, Souma S, Nakayama K, Trang C X, Sato T, Takahashi T and Ando Y 2016 *Phys. Rev. B* **94** 121108
[26] He J, Kong X, Wang W and Kou S P 2018 *New J. Phys.* **20** 053019
[27] Chang T Y, Pletikosic I, Kong T, *et al.* 2019 *Adv. Sci.* **6** 1800897
[28] Wang X T, Cheng Z X, Zhang G, *et al.* 2020 *Phys. Chem. Chem. Phys.* **22** 13650
[29] Kondo J 1964 *Prog. Theor. Phys.* **32** 37
[30] Gonzalez-Buxton C and Ingersent K 1998 *Phys. Rev. B* **57** 14254
[31] Fritz L and Vojta M 2004 *Phys. Rev. B* **70** 214427
[32] Vojta M and Fritz L 2004 *Phys. Rev. B* **70** 094502
[33] Sun J H, Wang L J, Hu X T, Li L and Xu D H 2018 *Phys. Rev. B* **97** 035130
[34] Wang L J, Hu X T, Li L, Xu D H, Sun J H and Chen W Q 2019 *Phys. Rev. B* **99** 235108
[35] Gunnarsson O and Schönhammer K 1983 *Phys. Rev. Lett.* **50** 604
[36] Varma C M and Yafet Y 1976 *Phys. Rev. B* **13** 2950
[37] Aji V, Varma C M and Vekhter I 2008 *Phys. Rev. B* **77** 224426
[38] Feng X Y, Chen W Q, Gao J H, Wang Q H and Zhang F C 2010 *Phys. Rev. B* **81** 235411
[39] Sun J H, Xu D H, Zhang F C and Zhou Y 2015 *Phys. Rev. B* **92** 195124
[40] Deng Y H, Lü H F, Ke S S, Guo Y and Zhang H W 2018 *J. Phys.: Condens. Matter* **30** 435602
[41] Lü H F, Deng Y H, Ke S S, Guo Y and Zhang H W 2019 *Phys. Rev. B* **99** 115109
[42] Ma D, Chen H, Liu H W and Xie X C 2018 *Phys. Rev. B* **97** 045148
[43] Chen R, Zhou B and Xu D H 2018 *Phys. Rev. B* **97** 155152
[44] Chan C K, Oh Y T, Han J H and Lee P A 2016 *Phys. Rev. B* **94** 121106
[45] Yan Z B and Wang Z 2016 *Phys. Rev. Lett.* **117** 087402
[46] Jiang J H and Wu S 2011 *Phys. Rev. B* **83** 205124
[47] Deng K, Wan G L, Deng P, *et al.* 2016 *Nat. Phys.* **12** 1105
[48] Ishii H 1978 *J. Low Temp. Phys.* **32** 457
[49] Barzykin V and Affleck I 1998 *Phys. Rev. B* **57** 432